Synthesis of PtSn₄ Intermetallic Nanodisks Through Galvanic Replacement Mechanism

Jiaqi Yu,[†] Shen-Wei Yu,[‡] Zhiyuan Qi,[†] Xiaotian Fang,[△] Tae-Hoon Kim,^{△, §} Lin Zhou,[△] Sen Zhang,^{‡, *} Wenyu Huang^{†, △, *}

†Department of Chemistry, Iowa State University, Ames, Iowa 50011, United States

KEYWORDS colloidal synthesis, growth mechanism, aberration-corrected transmission electron microscope, electroreduction, furfural, furfuryl alcohol

ABSTRACT: Intermetallic compounds with ordered crystal structures are attractive materials with extensive applications in many fields. PtSn₄, the most Sn-rich Pt-Sn intermetallic compound discovered so far, has special physical and catalytical properties because of the "Sn-Pt-Sn" layered crystal structure. However, studies on the properties of PtSn₄ have been limited to the single crystal due to the lack of success in preparing PtSn₄ nanomaterials. Here, starting from Sn nanoparticles, we demonstrated the preparation of monodisperse pure-phase PtSn₄ intermetallic nanodisks (PtSn₄ NDs) based on a galvanic replacement mechanism. The structure of as-synthesized PtSn₄ NDs was carefully characterized and analyzed. A systematic study on the PtSn₄ formation mechanism and kinetics confirms that the galvanic replacement mechanism governs the formation of PtSn₄ NDs. In electrocatalytic furfural reduction, PtSn₄ NDs effectively suppress the major competitive hydrogen evolution reaction and show superior faradaic efficiency than Pt nanoparticles.

INTRODUCTION

Intermetallic compounds, a type of metal alloy with a defined stoichiometry and ordered crystal structure, have attracted great interest in numerous fields. In catalysis. intermetallic compounds have become attractive candidates due to enhanced activity, selectivity, and durability compared with pure metals and disordered metal alloys.¹⁻³ Pt-Sn intermetallic compound is an important intermetallic system for catalysis because Pt as a noble metal plays a crucial role in many catalytic reactions, such dehydrogenation,4-5 hydrogenation,6-7 electrocatalytic reactions,8 while alloying with Sn, an abundant metal, improves the catalytic properties of Pt significantly.9 There are five reported Pt-Sn intermetallic compound phases, Pt₃Sn, Pt₃Sn₂, PtSn, PtSn₂, and PtSn₄. Among them, the most Sn-rich phase, PtSn₄, was reported as a topological material with Dirac node arcs, which has ultrahigh magnetoresistivity and carrier mobility. 10-12 PtSn₄ single crystal shows high activity and low overpotential in hydrogen evolution reaction (HER) due to its ultra-low resistance contributed by the high density of conduction electrons and Dirac node arcs.¹³ According to surface science studies on bulk PtSn4, the "Sn-Pt-Sn" layered structure in the PtSn₄ crystal enhances the poisoning resistance of PtSn₄, which could improve the durability of Pt in catalytic reactions. 14-15 With high carrier mobility, low resistivity, and enhanced anti-poisoning, PtSn4 is a promising candidate for catalysis, especially in electrocatalytic reactions.

Although intermetallic compounds are more stable compared to metal alloys, the formation of ordered intermetallic structures usually requires high energy input to overcome the barrier and facilitate kinetics for the structural transformation from disorder to order.¹⁶ Hightemperature annealing or reduction are commonly used to realize this structural transformation but can hardly control the morphology of intermetallic nanomaterials. Besides, the high-temperature annealing barely leads to the successful synthesis of low-temperature stable or metastable intermetallic nanomaterials but instead the formation of more stable or mixed intermetallic phases. PtSn₄ is the lowtemperature stable phase in the Pt-Sn intermetallic system. The preparation of pure-phase PtSn₄ nanomaterials is very challenging due to the competition with other phases, which has not been successfully demonstrated to the best of our knowledge.17-19

Most of the reported methods for synthesizing Pt-Sn intermetallic NPs start with Pt NP seeds that catalyze the reduction of Sn ions with polyol as the reducing agent, which prevents the formation of free Sn nanoparticles (NPs).²⁰⁻²¹ However, Sn-rich Pt-Sn intermetallic NPs, especially pure-phase PtSn₄ intermetallic NPs, can rarely be

^{*}Department of Chemistry, University of Virginia, Charlottesville, Virginia 22904, United States

⁴Ames Laboratory, The U.S. Department of Energy, Ames, Iowa 50011, United States

synthesized from Pt NP seeds using this method. ^{18,22} To access Sn-rich Pt-Sn intermetallic phases, it is natural to start with Sn NP seeds and control the amount of Pt that will be reduced and incorporated. ²³ We envision that a galvanic replacement reaction between Pt ions and metallic Sn seeds is an ideal method to localize the reduction of Pt to be only at the Sn NP surface, avoiding the formation of free Pt NPs. Another benefit of this method is that the reaction does not need to use other reducing agents. Galvanic replacement is a template-directed growth approach in colloidal synthesis, in which metal ions with a higher reduction potential in solution oxidize and simultaneously replace metal atoms with a lower reduction potential on template. ²⁴ Metal and metal oxide nanomaterials with various shapes and structures have been produced via galvanic replacement. ²⁵⁻

Herein, we demonstrated the controllable preparation of monodispersed pure-phase PtSn₄ intermetallic nanodisks (PtSn₄ NDs) in a colloidal synthetic system. The structure of PtSn₄ NDs was carefully confirmed from two crystal directions using high-resolution high-angle annular darkfield scanning transmission electron microscopy (HAADF-STEM). The galvanic replacement mechanism was revealed as the dominant growth mechanism based on the timedependent structure and composition evolution studies. Other synthesis conditions, such as the Pt precursor amount and addition rate, were also studied to explore the key parameters for growing monodisperse PtSn₄ NDs. Hybrid PtSn₄-Sn nanomaterials and PtSn₄-Sn-PtSn₄ "sandwich" structured nanomaterials can be synthesized as derivatives of the PtSn₄ synthetic system. The as-synthesized PtSn₄ NDs can serve as an ideal platform for electrochemical hydrogenation reaction owing to the "Sn-Pt-Sn" layered structure. As a proof-of-concept electrocatalysis application, PtSn₄ NDs enhance the selectivity and faradaic efficiency (FE) of electrocatalytic reduction of furfural (FF) to furfuryl alcohol (FA) compared with pure Pt and Sn NPs.

RESULTS AND DISCUSSION

We synthesized PtSn₄ NDs via a one-pot, two-step hot injection method. The Sn NPs were firstly prepared in the oleylamine (OAm). Following that, platinum precursor solution, platinum (II) acetylacetonate (Pt(acac)₂) dissolved in OAm, was added dropwise (0.25 mL min⁻¹) to form the PtSn₄ NDs. During this process, galvanic replacement happened between Sn NPs and Pt²⁺. Driven by the electrochemical potential difference, Sn atoms transfer electrons to Pt ions, and Pt ions are reduced and plated onto Sn NPs. The whole synthetic process was performed under an oxygen-free and moisture-free environment to prevent Sn from oxidation.

Transmission electron microscopy (TEM) and powder X-ray diffraction (PXRD) were conducted to characterize the morphology and crystal structure of PtSn₄ NDs. As shown in Figures 1a and b, the starting template, Sn NPs, shows uniform spherical shape with an average diameter of 22.6 ± 2.0 nm. With the addition of Pt(acac)₂ solution, the morphology of prepared NPs changes from sphere to disk. As shown in Figure 1c and d, some PtSn₄ NDs self-assemble with each other through plane-to-plane stacking, which present a rod shape from the side-view of NDs, while others

lay on the grid displaying a cubic morphology. The length and the thickness of PtSn₄ NDs are 18.2 \pm 1.5 nm and 9.2 \pm 1.2 nm, respectively, which were calculated by randomly measuring 100 self-assembled NDs. The PXRD patterns identify the crystal structure of the Sn NPs and PtSn₄ NDs (Figure 1e). Sn NPs have the β -Sn crystal structure with domain size of 27 nm estimated from Scherrer equation. The PXRD pattern of PtSn₄ NDs agrees with the theoretical PtSn₄ intermetallic compound. The peaks at 20 = 15.5 and 21.1° are typical intermetallic peaks corresponding to (020) and (111) planes of PtSn₄ crystal structure. The PtSn₄ domain size of PtSn₄ NDs calculated based on PXRD pattern is 16 nm, consistent with TEM analysis.

The HAADF-STEM images obtained from probe aberrationcorrected STEM in Figure 2 demonstrate the structural details of the

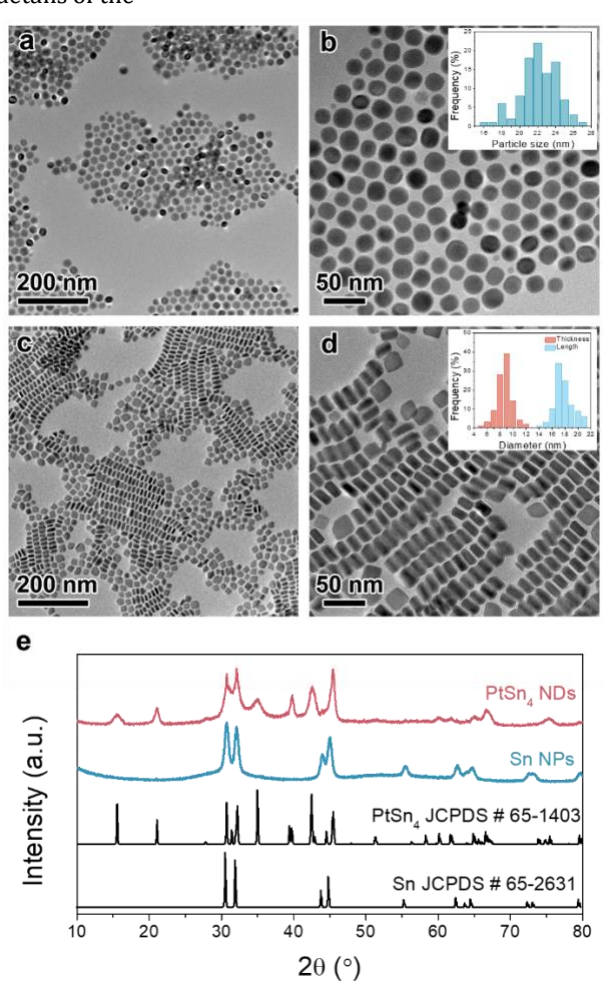


Figure 1. Structure and morphology characterizations of Sn NPs and PtSn₄ NDs. (a,b) TEM images of Sn NPs; insert: histogram of Sn NPs diameter; (c,d) TEM images of PtSn₄ NDs; insert: histogram of length (blue) and thickness (red) of PtSn₄ NDs; (e) PXRD pattern of Sn NPs (blue) and PtSn₄ NDs (red); black patterns: standard XRD pattern of PtSn₄ (JCPDS # 65-1403) and β-Sn (JCPDS # 65-2631).

PtSn₄ NDs. Figure 2a displays the self-assembled PtSn₄ NDs in two directions, showing both side plane and basal plane. High-resolution STEM (HR-STEM) images in Figures 2b and c provide zoom-in views from the two directions. As shown in Figure 2b, the lattice spacings of the PtSn₄ ND are 0.23

and 0.32 nm, which corresponds to (002) and (202) planes of PtSn₄. The fast Fourier transform (FFT) image shows the lowest index pattern of (002), (202), and (200), suggesting that the image is obtained through the [010] zone axis of PtSn₄ crystal. The layer-to-layer distance of Sn-Pt-Sn measured from Figure 2c is 0.57 nm, half of the PtSn₄ lattice parameter along [010] direction. The FFT of HR-STEM image of the NDs exhibiting side plane presents the lowest index diffraction pattern of (200), (020), and (220), which matches the pattern of PtSn₄ crystal from the [001] zone axis. The HR-STEM images obtained from [010] and [001] are compared with the crystal structure models of PtSn4 in both directions. From Figures 2e and f, the characteristic PtSn₄ layers display a "sandwich" structure containing "Sn-Pt-Sn" layers. The "Sn-Pt-Sn" layers are the essential structure affecting catalytic properties, which will be discussed later. The projection of the PtSn₄ from [010] direction includes four Sn atoms encapsulated in a square that is composed of Pt atoms at four corners. Therefore, the

vacancies (in green circle) existing at the edge of the prepared PtSn₄ NDs. These defects are likely caused by the oxidation of Sn after air exposure. In addition, to determine the distribution of Pt and Sn elements in PtSn₄ NDs, the HAADF-STEM energy-dispersive X-ray spectroscopy (EDS) elemental mapping was performed (Figure 2d). The EDS mapping shows the uniform distribution of Pt and Sn in the PtSn₄ NDs, and the atomic ratio of Pt to Sn is 18.4% to 81.6%, close to 1/4, which further proves the formation of PtSn₄ structure (EDS spectrum in Figure S1).

To understand the growth mechanism of PtSn₄ NDs, a time-dependent experiment was performed during the addition of Pt precursor, in which 0.2 mL aliquots were withdrawn at different intervals during the synthesis process. From TEM images, when a small amount of Pt precursor was added to Sn NPs, some particles have a dark layer or layers appear at the edge of the sphere-shaped Sn NPs (illustrated in blue circle, Figure 3a). As we discussed above, the PtSn₄ crystal shows "Sn-Pt-Sn" layered structure from [010]

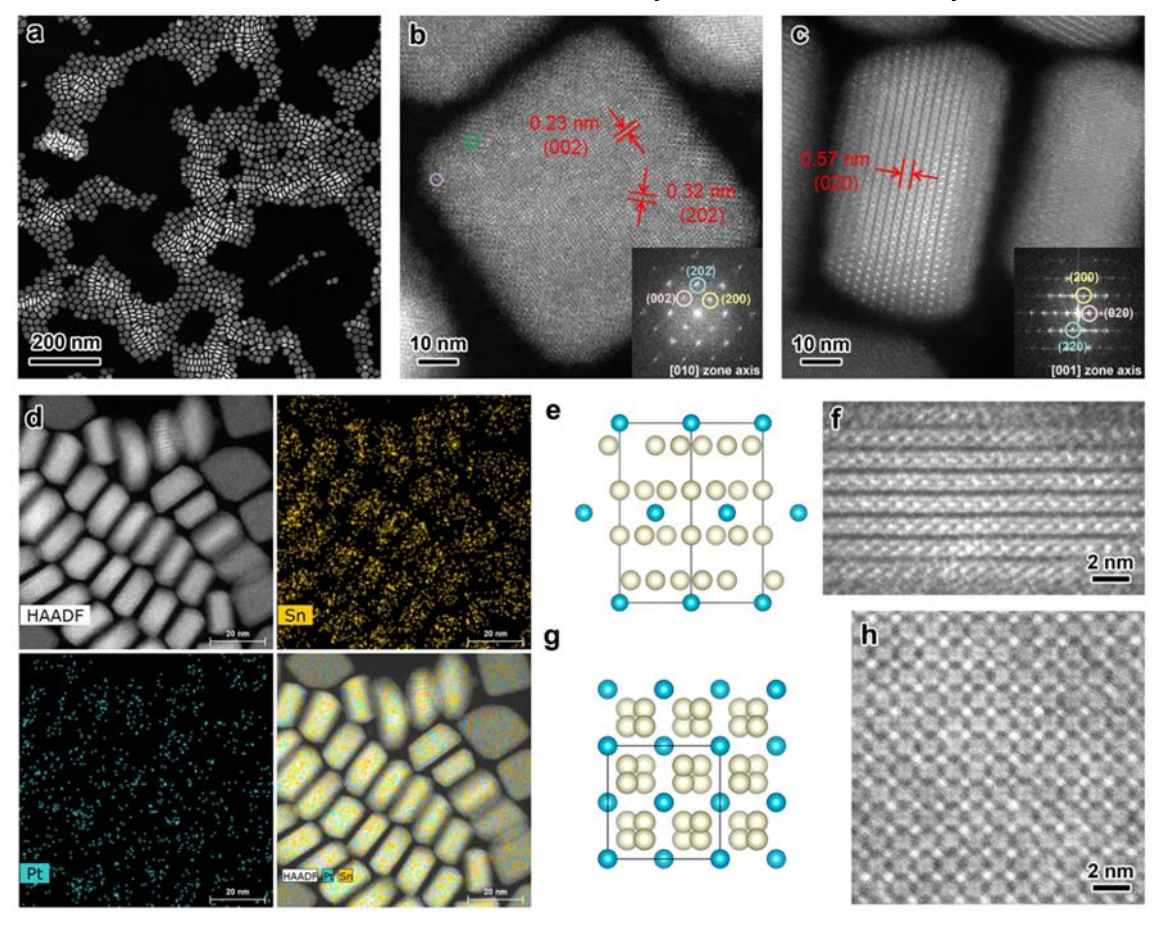


Figure 2. Detail structure characterization of PtSn₄ NDs. (a) STEM image of the PtSn₄ NDs; (b) HAADF HR-STEM images of the PtSn₄ NDs presenting the basal plane; green, Sn vacancy, purple, Pt substitution; (c) HAADF HR-STEM images of the PtSn₄ NDs presenting the side plane; inserts are the corresponding FFT images; (d) EDS-mapping of the PtSn₄ NDs; yellow Sn; blue Pt; scale bar 20 nm; (e, f) crystal model and HR-STEM of PtSn₄ structure viewing from [010] direction; (g, h) crystal model and HR-STEM of PtSn₄ structure viewing from [001] direction; blue Pt; yellow Sn.

lattice structures of PtSn₄ NDs viewed from both directions are consistent with the PtSn₄ crystal structure, as confirmed with HR-STEM (Figure S4) and EDS mapping (Figure S5). A careful analysis of lattice in Figure 2b reveals some defects, including Pt substitutions (in purple circle) and Sn

direction, so the dark layers on the edge of Sn NPs indicate the formation of PtSn $_4$ structure (shown in Figure 3b). With adding more Pt(acac) $_2$ /OAm precursor solution, the PtSn $_4$ layers grew thicker while the Sn part became smaller. Some particles formed the "sandwich" structure, with two PtSn $_4$

layers connected by Sn (shown in Figure 3c), which could result from the formation of two Pt nucleation points on the same Sn NP. When the Pt to Sn ratio reached 1/5 in the synthetic system, one Sn NP converted to one large PtSn₄ ND or two small PtSn₄ NDs, depending on the number of PtSn₄ nucleation on a single Sn NP. The time-dependent study shows that the size of Sn declines while the PtSn₄ size increases with time (Figure S2). During the time-dependent study, NPs were separated by centrifugation, and the inductively coupled plasma-mass spectrometry (ICP-MS) measurement was performed on the separated NPs to quantify the evolution of Pt to Sn ratio (Figure 3f). During the PtSn₄ NDs formation process, the amount of Sn in the particles decreased while the amount of Pt and the ratio of Pt/Sn increased simultaneously. Before adding Pt, the amount of Sn in Sn NPs was 2.1 mmol. With the addition of Pt, the amount of Sn dropped to 1.8 mmol, and the amount of Pt reduced and incorporated into Pt-Sn NPs was 0.3 mmol. The final ratio of Pt to Sn reached 0.18, which agrees with the EDS quantification result. From the PXRD patterns of the time-dependent samples (Figure S3), the peaks at 2θ =43.9° and 44.9° that belong to β -Sn became weaker. Meanwhile, the peaks at 35.0° and 42.5°, characterizing PtSn₄, kept increasing during the reaction. This timedependent study suggests that a galvanic replacement growth mechanism governs the formation process of PtSn₄ NDs from Sn NPs.

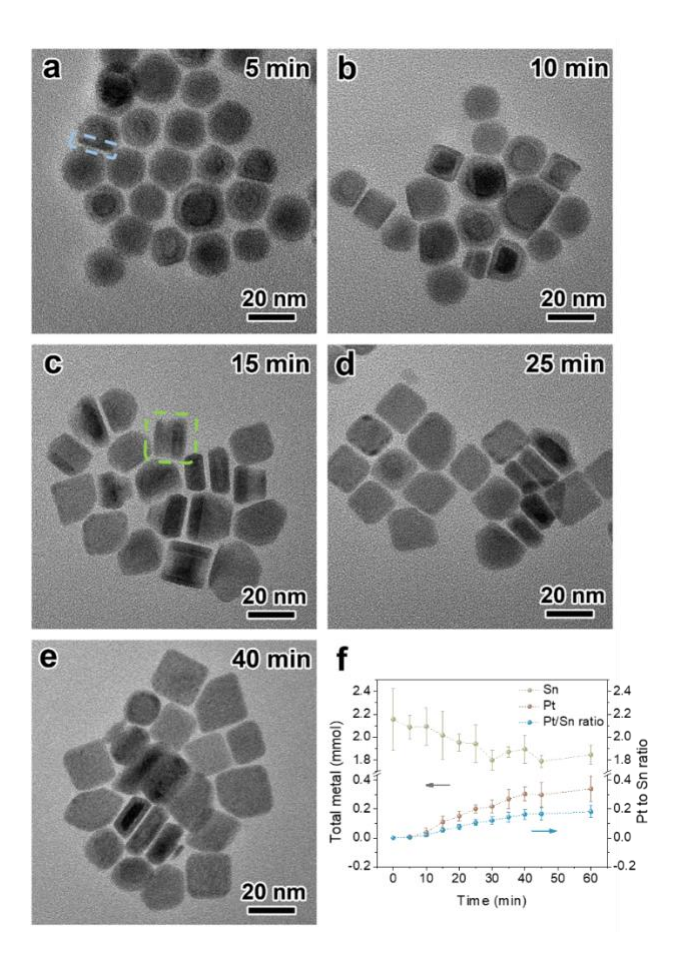


Figure 3. Time-dependent study on the formation of PtSn₄ NDs. (a-e) TEM images of the intermediate during Pt ion solution addition at 5 min, 10 min, 15 min, 25 min, and 40 min;

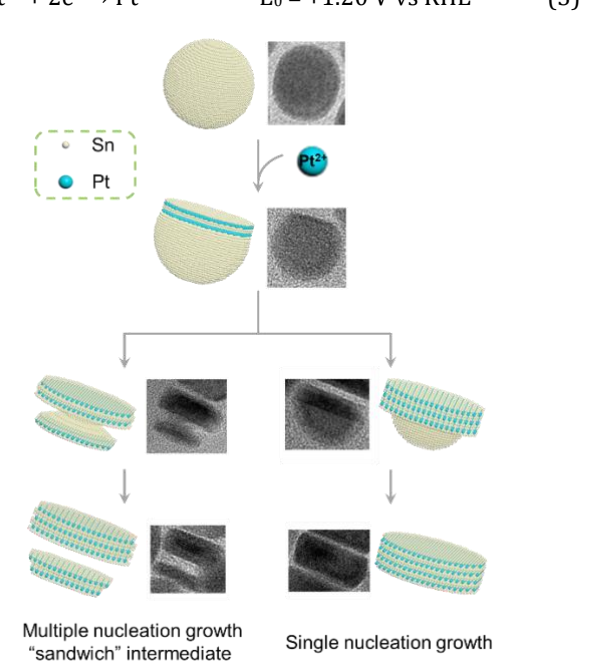
Blue circle PtSn₄ layers; green circle "sandwich" PtSn₄-Sn-PtSn₄ NP; (f) ICP-MS results of the time-dependent experiment. Green Sn amount; brown Pt amount; blue Pt to Sn ratio of the precipitate NPs.

Galvanic replacement occurs between active metal (low reduction potential) and less active metal ions (high reduction potential), in this case between Sn metal and Pt ions. Driven by the electrochemical potential difference of metals, the active metal transfers the electrons to and reduces the less active metal ion. The standard electrochemical reduction potentials of Pt and Sn ions are listed in equations (1) to (3). The reduction potential of both Sn²⁺ (-0.14 V vs. reversible hydrogen electrode, RHE) and Sn^{4+} (+0.15 V vs. RHE) is more negative than Pt^{2+} (+1.20 V vs. RHE), so the Sn metal in the synthetic system can be oxidized to both Sn²⁺ and Sn⁴⁺ ions. During the PtSn₄ NDs formation process, the Pt²⁺ ions reach the surface of Sn NPs and accept electrons from Sn atoms with the electrochemical potential as the driving force. Following that, the oxidized Sn ions leave the Sn NPs, and the reduced Pt atoms are plated on Sn NPs. The intermetallic PtSn₄ phase forms after rearrangement of Pt and Sn atoms in NPs driven by the negative formation enthalpy of the ordered phase. As shown in Scheme 1, the replacement of Sn with Pt happens at a particular point on the surface of Sn NPs, and then the PtSn₄ layers continue to grow from the replacement point. Occasionally, the PtSn₄ nucleation can happen at two spots on Sn NPs, resulting in the "sandwich" structures.

$$Sn^{2+} + 2e^{-} \rightarrow Sn$$
 $E_0 = -0.14 \text{ V vs RHE}$ (1)

$$Sn^{4+} + 2e^- \rightarrow Sn^{2+}$$
 $E_0 = +0.15 \text{ V vs RHE}$ (2)

$$Pt^{2+} + 2e^{-} \rightarrow Pt$$
 $E_0 = +1.20 \text{ V vs RHE}$ (3)



Scheme 1. Transformation of Sn NPs to PtSn₄ NDs. Right pathway: single point nucleation of PtSn₄ on Sn NP; Left pathway: two points nucleation and "sandwich" structure PtSn₄-Sn-PtSn₄ intermediate formed.

To have a comprehensive insight into the PtSn₄ NDs synthetic system, the addition rate of Pt precursor is studied as a critical kinetics parameter. Increased addition rates of Pt(acac)₂/OAm precursor solution, from 1 mL min⁻¹ to 5 mL s⁻¹, were conducted. When adding Pt solution at 1 mL min⁻¹, the final product presents the PtSn₄ dominant structure and disk morphology similar to the original slow addition, 0.25 mL min⁻¹, while the nanodisks are less monodispersed from TEM images with thickness of 8.7 ± 1.4 nm and length of 24.0 ± 2.9 nm (Figure 4a, S6). The formation of polydisperse nanodisks with the elevated addition rate can be explained from the time-dependent study that monitors the intermediate states. With faster addition rate, the nucleation and growth processes are poorly controllable, which leads to different degrees of galvanic replacement on different Sn NPs and high probability of forming multiple nucleation sites on single Sn NPs. Over 82% "sandwich" structured NPs generated as the intermediate (shown in Figure S7) of 1 mL min⁻¹ addition rate. From the "sandwich" structured NPs, the Sn part connecting two PtSn₄ layers shrank and focused on the center. Due to the uncontrollable growth process, the growth rate of PtSn₄ on the two sides of "sandwich" intermediate was different, resulting in two PtSn₄ NDs with different lengths and thicknesses. Further increasing the addition rate to 5 mL s-1 resulted in Sn dominant Pt-Sn NPs from PXRD, which means that not all the Pt ions are incorporated into Sn NPs to form PtSn₄ NDs. Small Pt clusters were observed in the HR-STEM images (Figure 4b, S9). The study on the addition rate of Pt precursor suggests that the addition rate as a reflection of kinetics has a significant effect on the intermediates and the final products. Higher addition rate of Pt precursors leads to multiple nucleation sites on Sn seeds, and the highest injection rate will cause self-nucleation of Pt.

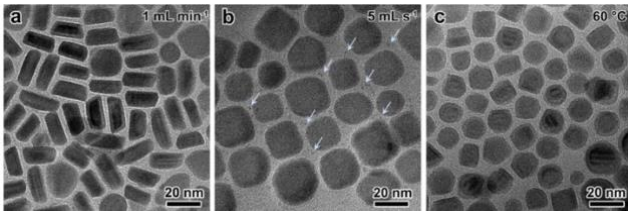


Figure 4. TEM images of Pt-Sn nanomaterials produced in the kinetics study of PtSn₄ synthetic system. (a) TEM image of PtSn₄ NDs formed with 4 times,1 mL min⁻¹, Pt precursor addition rate; (b) TEM image of products formed with quick injection, 5 mL s⁻¹; light blue arrow, Pt clusters; (c) TEM image of hybrid PtSn₄-Sn intermetallic-metal NPs formed when Pt precursor added at 60 °C.

Temperature is a key factor in colloidal synthesis, especially in intermetallic formation process.²⁹ As mentioned above, high temperatures (over 500 °C for some Pt-Sn intermetallic nanomaterials) are usually required to overcome the energy barriers for forming atomic ordering. In the developed galvanic replacement synthetic system, the PtSn₄ intermetallic phase was formed under mild temperatures, from 60 °C to 120 °C. As shown in Figure 4c, at 60 °C, PtSn₄ intermetallic layered structure appeared at the edge of Sn NPs template. Due to the sluggish kinetics at low temperature, part of Pt ions involved in the formation

of PtSn₄ intermetallic and hybrid PtSn₄-Sn intermetallic-metal NPs are prepared. Hybrid nanomaterials with anisotropic structure are attractive materials in many applications such as catalysis,³⁰⁻³¹ self-assemble,³² and cancer therapy.³³

To explore the possibilities of synthesizing Pt-Sn nanomaterials with different shapes or intermetallic phases, various Pt to Sn ratios, including 1/10, 1/5, and 1/2, were attempted. From Figure S10, the PXRD of Pt-Sn nanomaterial with Pt/Sn 1/10 ratio shows a mixture phase of Sn and PtSn₄. From the TEM images (Figure S11a, d), the 1/10 ratio Pt-Sn NPs has an anisotropic hybrid structure, with a combination of PtSn₄ plates and Sn hemisphere. When the Pt to Sn ratio increases to the 1/2 ratio, instead of PtSn₂, PtSn, or other Pt rich intermetallic phase, only a pure PtSn₄ intermetallic phase pattern was observed in the PXRD. From the ICP-MS result, Pt to Sn ratio in the Pt-Sn 1/2 NDs is 0.23, which indicates that the excess Pt precursor stays unreacted in solution. Same as the 1/5 ratio, the TEM images of the 1/2 ratio sample show monodispersed PtSn₄ NDs (Figure S11c, f). No other Pt-Sn intermetallic phases can be formed suggests Sn in the PtSn₄ is stabilized by the intermetallic structure and remains unreactive in the galvanic replacement under tested synthesis conditions.

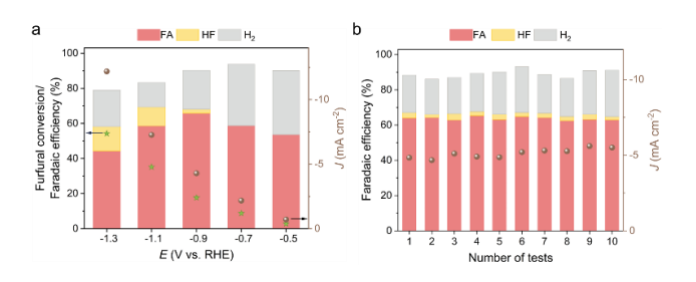


Figure 5. Performance of PtSn₄ NDs on electroreduction of furfural as a model catalytic reaction. (a) furfural conversion (green), total current density (brown), and FE to FA (red), HF (yellow), and grey (H₂) on PtSn₄ NDs at different potentials for 1h; (b) 10 cycles durability test on PtSn₄ NDs at –0.9 V vs. RHE, 1 h for each cycle; total current density (brown), and FE to FA (red), HF (yellow), and grey (H₂). All the electroreduction of furfural tests were performed in electrolyte containing 0.1 M FF and 0.1 M potassium phosphate buffer solutions (pH=7).

The special "Sn-Pt-Sn" layered structure along [010] direction determines special physical and catalytic properties of single crystal PtSn₄, including high conductivity, high carrier mobility, and enhanced antipoisoning. "Sn-Pt-Sn" layered structure also exists in the PtSn₄ NDs, so PtSn₄ NDs could have similar good conductivity and anti-poisoning properties with single crystal PtSn₄ and be a good electrocatalysts. We applied the PtSn₄ NDs to the electroreduction of furfural (FF) as a proofof-concept example to demonstrate the advantages of layer structured PtSn₄ NDs in catalysis. Electroreduction of FF is a model reaction for the transformative manufacturing of sustainable fuels and chemicals from biomass resources.34 The electroreduction of FF test was performed in buffer solution (0.1 M potassium phosphate buffer solutions (pH=7)) with 0.1 M FF under potential ranging from -0.5 V to -1.3 V vs. RHE (Figure 5a). Furfuryl alcohol (FA), the most appealing product from the conversion of FF due to the broad function in polymer resins, binders, coatings, fuels, and foundry industries, is the major product with PtSn₄ NDs as catalyst over the testing potential window. At -0.9 V vs. RHE, PtSn₄ shows the highest faradaic efficiency (FE), 65%, to FA, while the FE to FA on Pt NPs at -0.9 V vs. RHE is 35% and the hydrofuroin (HF) instead of FA is the major product on Sn NPs (Figure S13). The high selectivity and FE to FA suggest that although the PtSn₄ presents similar catalytic properties with Pt, the surface Sn from "Sn-Pt-Sn" layered structure, which prevents the direct exposure of Pt, is essential in impeding competitive reaction, HER. In addition, PtSn₄ NDs have good stability during the recycle test, which kept high FE and selectivity to FA and constant current density within 10 cycles (Figure 5b). This is consistent with the previous study that Sn layers enhanced the anti-poisoning capability of PtSn₄ single crystal compared to pure Pt. The TEM images of PtSn₄ after 10 cycle durability test shows the preservation of PtSn₄ NDs (Figure S15).

CONCLUSION

In conclusion, we prepared low-temperature stable Pt-Sn intermetallic nanomaterials, PtSn4 nanodisks, in a colloidal synthetic system. The crystal structure of PtSn₄ NDs presents the characteristic "Sn-Pt-Sn" layered structure, consistent with the single crystal PtSn₄ intermetallic structure. The formation of PtSn4 NDs from Sn NPs was dominated by the galvanic replacement, during which Pt ions were reduced by Sn and plated on the Sn NPs. Pt precursor addition rate and the galvanic replacement temperature are two critical kinetics parameters that affect the intermediates and the final products in the PtSn₄ synthetic system. Hybrid PtSn₄-Sn intermetallic-metal NPs were prepared as a derivative material at 60 °C. The assynthesized PtSn₄ NDs reached higher selectivity and FE to FA than Pt NPs in the electroreduction of furfural and effectively suppressed the competitive reaction, HER. Owing to the good conductivity and anti-poisoning properties determined by the "Sn-Pt-Sn" layered structure, PtSn₄ NDs could be an attractive alternative to Pt in many catalytic reactions, especially electrochemical catalysis. The developed synthetic approach, which starts with nonprecious metal NPs and forms intermetallic NPs via galvanic replacement, can be a general method to prepare intermetallic nanomaterials for application across fields.

EXPERIMENT

Materials

Lithium bis(trimethylsilyl)amide (LiN(SiMe₃)₂, 97%, Aldrich), oleic acid (OA, 90%, Aldrich), Tin (II) chloride (SnCl₂, anhydrous, 98%, BTC), tetrachloroethylene (TCE, ≥99%, Aldrich), diisobutylaluminium hydride (DIBAH, 1.0 M solution in THF, Aldrich), oleylamine (OAm, techn., TCI), platinum (II) acetylacetonate (Pt(acac)₂, 98%, Acros Organics), Furfuryl alcohol (FA, 98%, Alfa Aesar), Furfural (FF, 99%, Acros Organics), methylfuran (MF, 99%, Acros Organics), polyvinylidene fluoride (PVDF), nmethylpyrrolidone (NMP) and Vulcan XC-72 (Cabot) were used as received. All synthesis operations were carried out

under vacuum or using an argon Schlenk line. Carbon paper (Toray paper 060) and Nafion membrane (Nafion 212) used in the electrochemical cell were purchased from Fuel Cell Store. Electrolyte solutions were prepared using 18.2 M Ω H $_2O$ (Millipore SAS).

Synthesis of the PtSn₄ NDs

PtSn₄ NDs were synthesized through a hot injection method. Typically, in a 250 mL three-neck flask, 100 g of OAm was degassed at 140 °C under vacuum for 1.5 h. After naturally cooling down to 50 °C, the flask was briefly opened, and 2.5 mmol of SnCl₂ powder was added under the flow of ultrahigh purity argon. The mixture was heated up to 140 °C and degassed for another 30 min, followed by backfilling argon. With the addition of SnCl₂, the clear OAm solution changed to light yellow color. In parallel, the LiN(SiMe₃)₂/toluene solution was prepared in a glovebox, during which 3.612 g of LiN(SiMe₃)₂ was dissolved in 12 mL of dry toluene. At 210 °C, 10 mL of LiN(SiMe₃)₂/toluene solution was injected into the flask. After 10 s, 3.0 mL of DIBAH/THF (1 M DIBAH in THF) solution was injected rapidly. The color of the mixture turned dark brown immediately after adding the DIBAH reductant solution. In another 50 °C oil bath, a Pt precursor solution was prepared by dissolving Pt(acac)2 in OAm and degassing under vacuum. After 6 h at 210 °C, the Sn NPs solution was cooled to 120 °C, and the Pt/OAm precursor solution was added dropwise with the injection rate of 0.25 mL min⁻¹ (10 mL, 40 min total), which was precisely controlled by a syringe pump. The Pt-Sn mixture was kept at 120 °C for 1 h and then cooled to room temperature using a 25 °C water bath. After cooling to 40-50 °C, ~100 mL of ethanol (200 proof) was added to help precipitate the NPs. The mixture was centrifuged at 8000 rpm (8157 \times g) for 4 min and redispersed in 30 mL of oleic acid/TCE solution (2.4 mL of oleic acid in 120 mL of TCE solution) for ligand exchange. After ligand exchange, PtSn₄ NDs were precipitated by adding ~120 mL of ethanol and centrifugation (8157 × g). Finally, the PtSn₄ NDs were dispersed and stored in TCE. The heating of the reaction system was controlled by heating mantle with K-type thermocouple. The thermocouple wire was protected by a glass finger and inserted into the synthesis suspension.

Sn NPs were synthesized with a similar procedure to PtSn₄ NDs synthesis. After 6 h reaction at 210 °C, the mixture was directly cooled to room temperature using an ice water bath, followed by centrifugation and ligand exchange.

Characterization

TEM images were taken using a TECNAI G2 F20 operated at 200 kV. HAADF-STEM imaging was performed on a Titan Themis 300 equipped with gun monochromator and probe spherical aberration (Cs) corrector operated at 200 kV. The EDS mapping data was collected with a Super-X EDX detector. PXRD was performed on a Bruker D8 Advance Twin diffractometer using Cu $K_{\alpha 1}$ radiation (40 kV, 40 mA, λ = 0.1541 nm). The ICP-MS results were obtained by Agilent 7700 ICP-MS. The samples were digested completely in boiling aqua regia and diluted to appropriate concentrations.

TEM images of PtSn₄ after electrochemical reactions were obtained on a FEI Tecnai Spirit (120 kV). Inductively

coupled plasma optical emission spectrometry (ICP-OES) analyses were conducted on a PerkinElmer Avio-200 ICP optical emission spectrometer to determine the metal loading on the carbon-supported catalysts.

Electrochemical reduction of furfural

Preparation of working electrode. A measured amount of dried catalyst, 10 wt.% of polyvinylidene fluoride (PVDF), and few drops of n-methylpyrrolidone (NMP) were mixed thoroughly and applied onto both sides of carbon paper (total 2 cm²). The Pt and Sn loading on carbon paper was kept at 0.375 and 0.95 mg cm⁻², respectively, for all PtSn₄ NDs. The Pt loading on carbon paper was kept at 0.375 mg cm⁻² for Pt/C catalyst, while the Sn loading for Sn/C catalysts was kept at 0.95 mg cm⁻².

The electrochemical reduction of FF was investigated in 0.1 M potassium PBS (pH=7) and 0.1 M furfural electrolyte solution for 1 hr at each applied potential, using an Autolab Potentiostat (PGSTAT128N, Metrohm AG), a PtSn₄/C, Pt/C and Sn/C working electrode (2.0 cm²), an Ag/AgCl (4M KCl) reference electrode, and a Pt gauze counter electrode. All potentials were reported vs. the reversible hydrogen electrode (RHE) and obtained through open circuit potential (OCP), which was 0.585 V.

$$E (vs RHE) = E (vs Ag/AgCl) + OCP$$
 (4)

During the electrolysis, N₂ was steadily supplied to the cathode compartment at a rate of 10 SCCM, and the gas phase effluent in the headspace of the cathode compartment was continuously introduced to a gas chromatograph (Shimadzu, GC2014). The liquid phase products from the H-cell (see Scheme S1) were analyzed using high-performance liquid chromatography (Shimadzu, LC20-AD) equipped with a C18 column (Luna Omega, Phenomenex) a photodiode array UV-Vis detector (Shimadzu, SPD-M20A) at 260 nm for furfural and 210 nm for all other products. Hydrofuroin was identified by ¹H-NMR and mass spectrometry and quantified by HPLC.

Faradaic efficiency to liquid product i (i = MF, FA, HF) was calculated by

$$FE_i = \frac{N_i Z_i F}{Q} \times 100 \%$$
 (5)

where N_i is the number of moles of product i, Z_i is the number of electrons transferred per molecule of product (4 for MF and 2 for FA and HF), F is the Faraday constant (96,485.3 C mol⁻¹), and Q is the total charge passed through the system.

The incremental amount of evolved H_2 (N_{H_2} , moles) was obtained from the GC measurement.

The instantaneous faradaic efficiency of H_2 (fe_{H_2}) was calculated by

$$FE_{H_2} = \frac{N_{H_2} Z_{H_2} F}{\Delta O} \times 100 \%$$
 (7)

where Z_{H_2} is the number of electrons transferred per molecule of H_2 (2), ΔQ is the incremental charge transferred during the time (t) required to fill the sampling loop.

ASSOCIATED CONTENT

Supporting Information.

EDS spectrum of PtSn₄ NDs, PXRD, TEM images, and histogram of samples in time-dependent study, TEM and PXRD of sample prepared in different injection rate and Pt to Sn ratio, electrochemical setup, electroreduction of FF with Pt and Sn NPs, and TEM images of catalysts before and after electroreduction of FF. This material is available free of charge via the Internet at http://pubs.acs.org.

AUTHOR INFORMATION

Corresponding Author

* Sen Zhang - Department of Chemistry, University of Virginia, Charlottesville, Virginia 22904, United; orcid.org/0000-0002-1716-3741; Email: sz3t@virginia.edu

* Wenyu Huang - Department of Chemistry, Iowa State University, Ames, Iowa 50011, United States; Ames Laboratory, U.S. Department of Energy, Ames, Iowa 50011, United States; orcid.org/0000-0003-2327-7259; Email: whuang@iastate.edu

Present Addresses

§Department of Materials Science and Engineering, Chonnam National University, Gwangju 61186, South Korea

Author Contributions

All authors have given approval to the final version of the manuscript.

Notes

The authors declare no competing financial interest.

ACKNOWLEDGMENT

This work is partially supported by NSF grant CHE-2108306/2108307 and the Trapp award from Iowa State University. S.Y. and S.Z. are supported by NSF CBET-2004808 and 4-VA collaborative research program. We thank Prof. Robert J. Angelici for valuable suggestions.

REFERENCES

- (1) Cheng, H.; Gui, R.; Yu, H.; Wang, C.; Liu, S.; Liu, H.; Zhou, T.; Zhang, N.; Zheng, X.; Chu, W.; Lin, Y.; Wu, H.; Wu, C.; Xie, Y., Subsize Pt-based intermetallic compound enables long-term cyclic mass activity for fuel-cell oxygen reduction. *Proc. Natl Acad. Sci. USA* **2021**, *118* (35), e2104026118.
- (2) Nakaya, Y.; Xing, F.; Ham, H.; Shimizu, K.-i.; Furukawa, S., Doubly Decorated Platinum–Gallium Intermetallics as Stable Catalysts for Propane Dehydrogenation. *Angew. Chem. Int. Ed.* **2021**, *60* (36), 19715-19719.
- (3) Gong, Y.; Wu, J.; Kitano, M.; Wang, J.; Ye, T.-N.; Li, J.; Kobayashi, Y.; Kishida, K.; Abe, H.; Niwa, Y.; Yang, H.; Tada, T.; Hosono, H., Ternary intermetallic LaCoSi as a catalyst for N2 activation. *Nat. Catal.* **2018**, *1* (3), 178-185.
- (4) Xing, F.; Nakaya, Y.; Yasumura, S.; Shimizu, K.-i.; Furukawa, S., Ternary platinum–cobalt–indium nanoalloy on ceria as a highly efficient catalyst for the oxidative dehydrogenation of propane using CO2. *Nat. Catal.* **2022**, *5* (1), 55-65.
- (5) Yan, H.; He, K.; Samek, I. A.; Jing, D.; Nanda, M. G.; Stair, P. C.; Notestein, J. M., Tandem In203-Pt/Al203 catalyst for coupling of propane dehydrogenation to selective H2 combustion. *Science* **2021**, *371* (6535), 1257-1260.
- (6) Tian, S.; Wang, B.; Gong, W.; He, Z.; Xu, Q.; Chen, W.; Zhang, Q.; Zhu, Y.; Yang, J.; Fu, Q.; Chen, C.; Bu, Y.; Gu, L.; Sun, X.; Zhao,

- H.; Wang, D.; Li, Y., Dual-atom Pt heterogeneous catalyst with excellent catalytic performances for the selective hydrogenation and epoxidation. *Nat. Commun.* **2021**, *12* (1), 3181.
- (7) Macino, M.; Barnes, A. J.; Althahban, S. M.; Qu, R.; Gibson, E. K.; Morgan, D. J.; Freakley, S. J.; Dimitratos, N.; Kiely, C. J.; Gao, X.; Beale, A. M.; Bethell, D.; He, Q.; Sankar, M.; Hutchings, G. J., Tuning of catalytic sites in Pt/TiO2 catalysts for the chemoselective hydrogenation of 3-nitrostyrene. *Nat. Catal.* **2019**, *2* (10), 873-881.
- (8) He, T.; Wang, W.; Shi, F.; Yang, X.; Li, X.; Wu, J.; Yin, Y.; Jin, M., Mastering the surface strain of platinum catalysts for efficient electrocatalysis. *Nature* **2021**, *598* (7879), 76-81.
- (9) Motagamwala, A. H.; Almallahi, R.; Wortman, J.; Igenegbai, V. O.; Linic, S., Stable and selective catalysts for propane dehydrogenation operating at thermodynamic limit. *Science* **2021**, *373* (6551), 217-222.
- (10) Marchenkov, V. V.; Domozhirova, A. N.; Semiannikova, A. A.; Makhnev, A. A.; Shreder, E. I.; Naumov, S. V.; Chistyakov, V. V.; Patrakov, E. I.; Perevozchikova, Y. A.; Marchenkova, E. B.; Huang, J. C. A.; Eisterer, M., Electrical and optical properties of a PtSn4 single crystal. *Journal of Physics: Conference Series* **2019**, *1199*, 012037.
- (11) Fu, C.; Guin, S. N.; Scaffidi, T.; Sun, Y.; Saha, R.; Watzman, S. J.; Srivastava, A. K.; Li, G.; Schnelle, W.; Parkin, S. S. P.; Felser, C.; Gooth, J., Largely Suppressed Magneto-Thermal Conductivity and Enhanced Magneto-Thermoelectric Properties in PtSn4. *Research* **2020**, *2020*, 4643507.
- (12) Wu, Y.; Wang, L.-L.; Mun, E.; Johnson, D. D.; Mou, D.; Huang, L.; Lee, Y.; Bud'ko, S. L.; Canfield, P. C.; Kaminski, A., Dirac node arcs in PtSn4. *Nature Physics* **2016**, *12* (7), 667-671.
- (13) Li, G.; Fu, C.; Shi, W.; Jiao, L.; Wu, J.; Yang, Q.; Saha, R.; Kamminga, M. E.; Srivastava, A. K.; Liu, E.; Yazdani, A. N.; Kumar, N.; Zhang, J.; Blake, G. R.; Liu, X.; Fahlman, M.; Wirth, S.; Auffermann, G.; Gooth, J.; Parkin, S.; Madhavan, V.; Feng, X.; Sun, Y.; Felser, C., Dirac Nodal Arc Semimetal PtSn4: An Ideal Platform for Understanding Surface Properties and Catalysis for Hydrogen Evolution. *Angew. Chem. Int. Ed.* **2019**, 58 (37), 13107-13112.
- (14) Bukhvalov, D.; Marchionni, A.; Filippi, J.; Kuo, C. N.; Fuji, J.; Edla, R.; Nappini, S.; D'Olimpio, G.; Ottaviano, L.; Lue, C. S.; Torelli, P.; Vizza, F.; Politano, A., Efficient electrochemical hydrogen evolution reaction with PtSn4 via surface oxidation. *J. Mater. Chem. A* **2019**, 8 (5), 2349-2355.
- (15) D'Olimpio, G.; Boukhvalov, D. W.; Fujii, J.; Torelli, P.; Marchionni, A.; Filippi, J.; Kuo, C.-N.; Edla, R.; Ottaviano, L.; Lue, C. S.; Vizza, F.; Nappini, S.; Politano, A., Catalytic activity of PtSn4: Insights from surface-science spectroscopies. *Appl. Surf. Sci.* **2020**, *514*, 145925.
- (16) Yang, C.-L.; Wang, L.-N.; Yin, P.; Liu, J.; Chen, M.-X.; Yan, Q.-Q.; Wang, Z.-S.; Xu, S.-L.; Chu, S.-Q.; Cui, C.; Ju, H.; Zhu, J.; Lin, Y.; Shui, J.; Liang, H.-W., Sulfur-anchoring synthesis of platinum intermetallic nanoparticle catalysts for fuel cells. *Science* **2021**, *374* (6566), 459-464.
- (17) Downing, D. O.; Liu, Z.; Eichhorn, B. W., Synthesis of PtSn4 and Ir3Sn7 intermetallic nanoparticles from bimetallic Zintl cluster precursors. *Polyhedron* **2016**, *103*, 66-70.
- (18) Erdt, A. J.; Gutsche, C.; Fittschen, U. E. A.; Borchert, H.; Parisi, J.; Kolny-Olesiak, J., Control of crystallographic phases and surface characterization of intermetallic platinum tin nanoparticles. *CrystEngComm* **2019**, *21* (21), 3363-3373.
- (19) DeSario, D. Y.; DiSalvo, F. J., Ordered Intermetallic Pt–Sn Nanoparticles: Exploring Ordering Behavior across the Bulk Phase Diagram. *Chemistry of Materials* **2014**, *26* (8), 2750-2757.

- (20) Bauer, J. C.; Chen, X.; Liu, Q.; Phan, T.-H.; Schaak, R. E., Converting nanocrystalline metals into alloys and intermetallic compounds for applications in catalysis. *J. Mater. Chem.* **2008**, *18* (3), 275-282.
- (21) Maligal-Ganesh, R. V.; Xiao, C.; Goh, T. W.; Wang, L.-L.; Gustafson, J.; Pei, Y.; Qi, Z.; Johnson, D. D.; Zhang, S.; Tao, F.; Huang, W., A Ship-in-a-Bottle Strategy To Synthesize Encapsulated Intermetallic Nanoparticle Catalysts: Exemplified for Furfural Hydrogenation. *ACS Catal.* **2016**, *6* (3), 1754-1763.
- (22) Cable, R. E.; Schaak, R. E., Reacting the Unreactive: A Toolbox of Low-Temperature Solution-Mediated Reactions for the Facile Interconversion of Nanocrystalline Intermetallic Compounds. *J. Am. Chem. Soc.* **2006**, *128* (30), 9588-9589.
- (23) Chou, N. H.; Schaak, R. E., Shape-Controlled Conversion of β-Sn Nanocrystals into IntermetallicM-Sn (M= Fe, Co, Ni, Pd) Nanocrystals. *J. Am. Chem. Soc.* **2007**, *129* (23), 7339-7345.
- (24) Skrabalak, S. E.; Chen, J.; Sun, Y.; Lu, X.; Au, L.; Cobley, C. M.; Xia, Y., Gold Nanocages: Synthesis, Properties, and Applications. *Accounts of Chemical Research* **2008**, *41* (12), 1587-1595.
- (25) Zhu, Y.; Zhang, X.; Koh, K.; Kovarik, L.; Fulton, J. L.; Rosso, K. M.; Gutiérrez, O. Y., Inverse iron oxide/metal catalysts from galvanic replacement. *Nat. Commun.* **2020**, *11* (1), 3269.
- (26) Sun, Y.; Xia, Y., Shape-Controlled Synthesis of Gold and Silver Nanoparticles. *Science* **2002**, *298* (5601), 2176-2179.
- (27) Oh, M. H.; Yu, T.; Yu, S.-H.; Lim, B.; Ko, K.-T.; Willinger, M.-G.; Seo, D.-H.; Kim, B. H.; Cho, M. G.; Park, J.-H.; Kang, K.; Sung, Y.-E.; Pinna, N.; Hyeon, T., Galvanic Replacement Reactions in Metal Oxide Nanocrystals. *Science* **2013**, *340* (6135), 964-968.
- (28) Castilla-Amorós, L.; Stoian, D.; Pankhurst, J. R.; Varandili, S. B.; Buonsanti, R., Exploring the Chemical Reactivity of Gallium Liquid Metal Nanoparticles in Galvanic Replacement. *J. Am. Chem. Soc.* **2020**, *142* (45), 19283-19290.
- (29) Clarysse, J.; Moser, A.; Yarema, O.; Wood, V.; Yarema, M., Size- and composition-controlled intermetallic nanocrystals via amalgamation seeded growth. *Sci. Adv.* **2021**, *7* (31), eabg1934.
- (30) Guan, B. Y.; Yu, L.; Lou, X. W., Formation of Asymmetric Bowl-Like Mesoporous Particles via Emulsion-Induced Interface Anisotropic Assembly. *J. Am. Chem. Soc.* **2016**, *138* (35), 11306-11.
- (31) Yu, J.; Kolln, A. F.; Jing, D.; Oh, J.; Liu, H.; Qi, Z.; Zhou, L.; Li, W.; Huang, W., Precisely Controlled Synthesis of Hybrid Intermetallic–Metal Nanoparticles for Nitrate Electroreduction. *ACS Appl. Mater. Interfaces* **2021**, *13* (44), 52073-52081.
- (32) Hu, H.; Ji, F.; Xu, Y.; Yu, J.; Liu, Q.; Chen, L.; Chen, Q.; Wen, P.; Lifshitz, Y.; Wang, Y.; Zhang, Q.; Lee, S. T., Reversible and Precise Self-Assembly of Janus Metal-Organosilica Nanoparticles through a Linker-Free Approach. *ACS Nano* **2016**, *10* (8), 7323-7330.
- (33) Hu, H.; Liu, J.; Yu, J.; Wang, X.; Zheng, H.; Xu, Y.; Chen, M.; Han, J.; Liu, Z.; Zhang, Q., Synthesis of Janus Au@ periodic mesoporous organosilica (PMO) nanostructures with precisely controllable morphology: a seed-shape defined growth mechanism. *Nanoscale* **2017**, *9* (14), 4826-4834.
- (34) Mariscal, R.; Maireles-Torres, P.; Ojeda, M.; Sádaba, I.; López Granados, M., Furfural: a renewable and versatile platform molecule for the synthesis of chemicals and fuels. *Energy & Environmental Science* **2016**, *9* (4), 1144-1189.

Table of Contents

